Impact of Martensite Spatial Distribution on Quasi-Static and Dynamic Deformation Behavior of Dual-Phase Steel

MANPREET SINGH, ANINDYA DAS, T. VENUGOPALAN,
KRISHNENDU MUKHERJEE, MAHESH WALUNJ, TARUN NANDA,
and B. RAVI KUMAR

The effects of microstructure parameters of dual-phase steels on tensile high strain dynamic deformation characteristic were examined in this study. Cold-rolled steel sheets were annealed using three different annealing process parameters to obtain three different dual-phase microstructures of varied ferrite and martensite phase fraction. The volume fraction of martensite obtained in two of the steels was near identical (~ 19 pct) with a subtle difference in its spatial distribution. In the first microstructure variant, martensite was mostly found to be situated at ferrite grain boundaries and in the second variant, in addition to at grain boundaries, in-grain martensite was also observed. The third microstructure was very different from the above two with respect to martensite volume fraction (~ 67 pct) and its morphology. In this case, martensite packets were surrounded by a three-dimensional ferrite network giving an appearance of core and shell type microstructure. All the three steels were tensile deformed at strain rates ranging from 2.7×10^{-4} (quasi-static) to 650 s^{-1} (dynamic range). Field-emission scanning electron microscope was used to characterize the starting as well as post-tensile deformed microstructures. Dual-phase steel consisting of small martensite volume fraction (~ 19 pct), irrespective of its spatial distribution, demonstrated high strain rate sensitivity and on the other hand, steel with large martensite volume fraction (~ 67 pct) displayed a very little strain rate sensitivity. Interestingly, total elongation was found to increase with increasing strain rate in the dynamic regime for steel with core–shell type of microstructure containing large martensite volume fraction. The observed enhancement in plasticity in dynamic regime was attributed to adiabatic heating of specimen. To understand the evolving damage mechanism, the fracture surface and the vicinity of fracture ends were studied in all the three dual-phase steels.

I. INTRODUCTION

FERRITE–MARTENSITE dual-phase (DP) steels are attracting a great demand in the automobile industries owing to their high strength-to-weight ratio, excellent formability, and high yield-to-ultimate strength ratio.[1,2] Moreover, being a potential material for the automobile component application, DP steels are studied extensively in order to evaluate and understand their plastic deformation characteristic in various loading conditions.[3–5] The difference in hardness of ferrite and martensite phases of DP steels provides various microstructure engineering opportunities in developing high-strength steels with excellent properties. Because of the complex microstructure (ferrite + martensite) constituents, the properties of DP steels are found to be influenced largely by the (a) volume fraction, (b) size and its distribution, and (c) morphology of the individual constituent phases.[6–10] Erdogan et al. reported that yield strength (YS) and ultimate tensile strength (UTS) increase for DP microstructure consist of fine martensite compared to blocky martensite in ferrite matrix.[11] On the other hand, martensite volume fraction noted to influence the ductility and the ductile void formation characteristics during plastic deformation.[12,13] Ductility was also found to be largely affected by the morphology of martensite. The fine fibrous or fine globular type martensite reported producing higher total elongation compared to coarser/

MANPREET SINGH and TARUN NANDA are with the Mechanical Engineering Department, Thapar University, Patiala 147004, India. ANINDYA DAS, KRISHNENDU MUKHERJEE, MAHESH WALUNJ, and B. RAVI KUMAR are with the CSIR-National Metallurgical Laboratory, Jamshedpur 831007, India. Contact e-mail: ravik_in@yahoo.com T. VENUGOPALAN is with Tata Steel Limited, Jamshedpur 831001, India.
Manuscript submitted June 23, 2017.
Article published online December 12, 2017

blocky type martensite.[13] Martensite morphology and its distribution were also reported to affect the fracture/damage mechanisms of DP steels.[14,15] In a recent work, Ravi et al.[16] produced a core–shell type martensite/ferrite DP microstructure by controlling austenite decomposition and found that microcracks initiated in martensite packets were arrested at the martensite/ferrite inter-phase boundaries. The network of ferrite channel around martensite retarded the crack growth and thereby delays the onset of global deformation. Therefore, ductility was found to increase in core–shell type morphology even with high volume fraction of martensite. All the above-discussed DP microstructure details enable one to understand the influence of microstructure parameters on mechanical properties of the DP steels. For automobile crashworthiness assessment, it becomes an absolute necessity to investigate the effect of these microstructure parameters on the deformation characteristics of DP steels at high strain rates.

The typical strain rate of deformation experienced during an event of automobile crash is around 100 to 500 s^{-1}. The effect of martensite volume fraction on the high strain rate tensile properties is well studied.[17–21] The martensite fraction is found to possess a positive influence on strength and energy absorption characteristics but exhibits a negative or little influence on the ductility of the steel. The strain hardening rates were observed to have a negative/an insensitive response to increasing strain rates.[20,21] The strain rate sensitivity of the DP steel was found to decrease with increase in martensite volume fraction.[17] Compared to the quasi-static strain rates, the rate of increase in strength is higher in the high strain rate regime.[22] Further, the strain incompatibility between soft ferrite and hard martensite causes inter-phase boundary decohesion. Inter-phase decohesion affects void nucleation rate and its growth and hence influences the damage mechanism. Therefore, the spatial distribution, size, and fraction of the martensite affect the dimple size in the fracture surface. For example, a lower volume fraction of martensite of DP600 steel compared to that of DP800 steel was reported causing the formation of larger dimple size at a strain rate of 800 s^{-1}.[22] Thus the influence of martensite fraction, size, and especially morphology not only affects their properties under the quasi-static strain rates of loading but also at high strain rates. The dimple size and its distribution are also found to be influenced by the strain rate. In view of the above, microstructure engineering can be employed in the development of a DP microstructure for high crash resistance properties.

Extensive research endeavors have been reported on high strain rate properties of DP steels. However, the effect of martensite morphology and its distribution on the tensile deformation characteristics has not been investigated at high strain rates, generally, encountered in automobile crash conditions. Thus, the present research was aimed to understand the effect of martensite morphology, and its distribution on the quasi-static and dynamic tensile deformation behavior of DP steels. Furthermore, the impact of martensite morphology on damage initiation and propagation mechanisms was

looked into. By controlling annealing process parameters, three different DP steel microstructures were produced for the present study.

II. EXPERIMENTAL DETAILS

A. Materials and Processing

Industrial cold-rolled steel sheets (67 pct thickness reduction) having a final thickness of 0.83 mm and with chemical composition shown in Table I were used in this study. This steel is used by the steel industry for the production of DP590 steel in continuous annealing process line. Steel sheets were subjected to three different types of annealing processes in a hot dip process simulator (HDPS, ICS Iwatani Surtec, Germany) to achieve desired engineered microstructures. The annealing process included (i) the conventional continuous annealing line process used in steel industry for producing DP590 grade steel (CAL),[9,10] (ii) the continuous heating and cooling resulting in modified DP microstructure (CHCL),[9,10] and (iii) the annealing process resulting in core and shell type DP microstructure (CAS).[16] The infrared heating mode was used for heating purposes, and a mixture of H$_2$ (10 vol pct) and N$_2$ (10 vol pct) gases was used for maintaining the annealing atmosphere and for cooling purposes. A k-type thermocouple was spot-welded to the specimen to get real-time temperature profile.

The schematic of annealing schedule employed for three different processes is shown in Figure 1. In CAL, the specimens were heated to 790 °C (1063.15 °K) at 10 deg/s followed by the isothermal holding of 60 seconds at this temperature. This was followed by fast cooling in three stages. The first stage was free cooling from 790 °C (1063.15 °K) to 675 °C (948.15 °K) for austenite enrichment with carbon. The second stage was ultra-fast cooling to 275 °C (548.15 °K) for the transformation of austenite to martensite. The third stage was holding at 275 °C (548.15 °K) for 120 seconds for the tempering of transformed martensite and finally quenching to room temperature. The conventional CAL process is reported to form DP microstructure with some preference of martensite formation at grain boundaries of ferrite.[9,10]

The CHCL process, a modification of the CAL process, was employed to get DP microstructure with the identical volume fraction of martensite with the difference in its spatial distribution. In CHCL process, different heating rates were used in three stages to reach peak annealing temperature. In the first stage, heating was continued up to 710 °C (983.15 °K) at a heating rate of 5 deg/s. In the second stage, the slower heating rate of 1 deg/s was employed to reach 790 °C (1063.15 °K). In the third stage, heating to 840 °C (1113.15 °K) was conducted at a heating rate of 2 deg/s. Finally, the cooling route similar to that of CAL process was followed. The metallurgical attributes by which the resultant DP microstructure was obtained in CHCL are discussed elsewhere.[9,10] The objective of CAS process was to obtain core- and shell-like DP microstructure

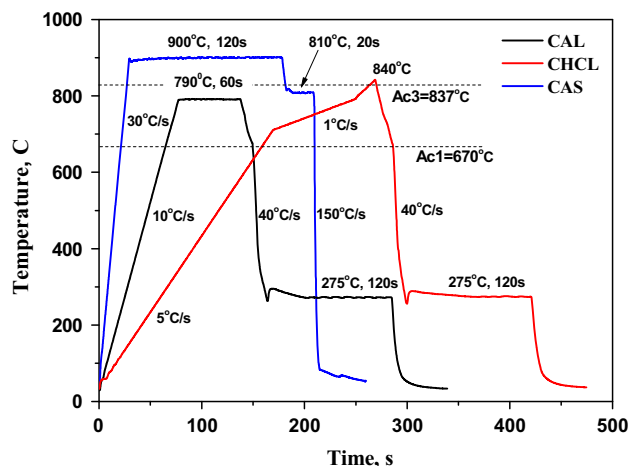| Element	C	Mn	P	S	Si	Al	N
Weight percent	0.074	1.83	0.012	0.002	0.43	0.026	0.0032

Fig. 1—Annealing cycles used in the present work for obtaining three different DP microstructures (Color figure online).

having martensite packets surrounded by three-dimensional ferrite network/channel. The underlying phenomenon of the evolution of such microstructure for CAS process, as shown in Figure 1, is reported elsewhere.[16]

B. Tensile Testing at Quasi-Static and High Strain Rates

Tensile tests at a quasi-static strain rate of 2.7×10^{-4} s^{-1} were performed on Instron 8862 system. The respective load cell of the system provided the load data, whereas an extensometer of 25 mm gage length was used to record the extension data. The quasi-static tensile tests were conducted according to the ASTM standard E8M.[23] For high strain rate tensile tests (100, 200, 500, and 650 s^{-1}), a high-speed servo-hydraulic Instron VHS 8800 test system was used. The load and strain data from high strain rate experiments were recorded using separate strain gages pasted on the surface of the specimens. The positioning of the strain gage and extraction of data from the strain gages was as per the methodology suggested by Wood and Schley.[24] The specimen dimensions for high strain rate tests were machined in accordance with ISO standard 26203-2.[25] The respective sample dimensions for quasi-static and high strain rate tests are shown in Figure 2.

C. Microstructure Characterization

FEG-SEM set-up (FEI Nova NanoSEM 430) was used for the microstructure characterisation. Microstructures in the as-processed as well as in post-deformed condition were analyzed to understand the distribution of phases and the extent of deformation of various microstructure constituents. Parameters such

as phase fraction and size distribution of constituent phases of the DP microstructures were determined through quantitative image analysis techniques by using ImageJ software (ImageJ 1.46 r; National Image Institute of Health, Wayne Rasband). Specimens from deformed steel were cut from the necked region to study the mechanisms of micro crack/damage evolution during tensile deformation. Microstructures were prepared using the standard metallographic technique. Fractography analysis was also conducted on the fracture surface to elucidate the fracture mechanisms.

III. RESULTS AND DISCUSSION

A. Initial Microstructures Obtained Through Various Annealing Processes

SEM micrographs of steel specimens obtained after processing by the three different annealing routes are shown in Figure 3. The microstructure obtained by CAL process consisted of ferrite matrix with martensite phase distributed mostly at the grain boundaries of ferrite, i.e., microstructure comprises ferrite and grain boundary martensite (see Figure 3(a)). For the CHCL process route, martensite formation tendency, in addition to at ferrite grain boundaries, was also within the ferrite grains or at 'in-grain' ferrite sites (Figure 3(b)). The microstructure consists mainly of ferrite matrix with martensite phase distributed both at the grain boundaries (grain boundary martensite) as well as within the ferrite grains (in-grain martensite). Both CAL and CHCL consisted of near identical fraction of martensite of about 19 pct in their respective microstructures. Quantitative microstructure analysis carried out by image analysis of microstructures showed differences in martensite size distribution between the two steels. In the case of CAL, size distribution was up to 1.5 μm^2 size range, whereas for CHCL it was limited to below 1.0 μm^2. On the other hand, microstructure obtained by CAS process consisted of core and shell type DP microstructure in which martensite core, in the size range of ~ 48 μm^2, was surrounded by three-dimensional ferrite network/channel (Figure 3(c)). Further, CAS steel possesses ~ 67 pct of martensite in the microstructure. Therefore, a shift from ferrite dominant microstructure to martensite dominant DP steel was produced. More details on all the three annealing processes and microstructure evolution mechanism can be found elsewhere.[9,10,16]

B. Tensile Properties at Different Strain Rates

1. At quasi-static strain rate
Figure 4 shows the comparison of the tensile deformation behavior of the three DP steels at the quasi-static

condition. The evaluated tensile properties are also shown in Table II. CAL and CHCL although show similar YS, but the UTS of CHCL was slightly higher than CAL with near comparable percentage of elongation. Compared to CAL, the CHCL-processed DP steel has some in-grain martensite along with grain boundary martensite, at near identical volume fraction of martensite. This subtle change in the microstructure due to an additional new morphology/in-grain martensite might have caused the increase in the tensile strength, with the almost same percentage of elongation. The presence of in-grain martensite crystals introduces additional strain hardening sites at ferrite grain interior along with at grain boundaries. These in-grain martensite particles, therefore, accelerate the evolution of dislocation density in the surrounding ferrite grain resulting in its rapid hardening. On the other hand, a remarkable increase in the strength can be seen for the CAS-processed steel owing to its large volume fraction of martensite (~ 67 pct).

2. At high strain rates

The three DP steels with different microstructure morphologies were subjected to tensile deformation at high strain rates (100 to 650/s). The engineering stress–strain curves at high strain rates superimposed with quasi-static strain rate curves for the three steels are shown in Figures 5(a) through (c). The cross-head velocities used to produce strain rates of 100 to 650/s were about 1.6 to 10.4 m/s. Such high-speed cross-head operation generates elastic waves which hit the piezo-electric load cell and cause load cell ringing. The ringing of the load cell during the high strain rate tensile deformation induces noise in the associated acquired load data. To circumvent this problem, strain gages were pasted on the specimen surfaces which do not experience such high ringing effect. Thus the data extracted using the strain gages have sufficiently less noise compared to that obtained from the load cell. Even with the application of strain gages, it is very much difficult to completely eliminate data noise. As a result, the high strain rate data have some amount of fluctuations, as can be seen in Figure 5. The evaluated strength and uniform elongation at different strain rates are shown in Figure 6. Certainly, the increment in strength with strain rate increase was high for CAL while the magnitude of increment gradually decreases for CHCL and CAS steels. The ductility was observed to decreases monotonically with an increase in strain rate for CAL and CHCL steels. However, this decrease was slightly smaller in the case of CHCL steel. An opposite behavior was observed for the CAS-processed steel where the elongation was found to increase remarkably as the strain rate was increased. The continuous increase in the elongation values for CAS steel indicates an underlying difference in plastic deformation mechanism due to core/shell type microstructure morphology.

From the flow curves obtained at different strain rates, the strain rate sensitivity of these steels at different strain levels was also analyzed. Figure 7 shows the variation of stress at different strain rates for true strain value of 0.05. The slope of the true stress and strain rate changes significantly at high strain rate. The strain rate sensitivity was high at high strain rates compared to quasi-static. Since at quasi-static strain rate tensile tests at only one strain rate was performed, the strain rate sensitivity in quasi-static regime is not reported here. Nevertheless, some previous literature has also reported about the increase in strain rate sensitivity at high strain rates in low carbon steels.[26,27] The CAS-processed steel showed the least strain rate sensitivity especially at high strain rates, whereas the CAL has exhibited the highest strain rate sensitivity in the dynamic regime. Strain rate sensitivity is largely influenced by the solid solution-hardened phases, like ferrite. Among the three steels studied, the CAS process produced microstructure containing predominantly martensite than of the other two. Martensite has the least affinity towards strain rate hardening because of its asymmetric crystal structure. Due to the asymmetry, few slip systems operate in martensite during deformation. Consequently, the glide of dislocations in martensite is heavily restricted which causes a brittle fracture. Furthermore, structure asymmetry also results in negligible interactions within the dislocations itself. As a result, hardening due to dislocation–dislocation interaction is very poor in the martensite phase compared to that of the ferrite phase. Therefore, even with an increase in strain rate, the strength of martensite does not increase in an appreciable manner, due to poor dislocation–dislocation interaction within the hard martensite phase. This is the reason for the stress increment of CAS-processed steel when strain rate increased was very small. Poor strain rate sensitivity of martensite has been reported by Bardelcik et al.[28] when a fully martensitic steel was deformed in tension at 0.003 and 960/s. It should also be noted that at dynamic strain rates, adiabatic heating of specimen plays a major role in the deformation process along with the strain hardening. Martensite phase has little strain hardening and strain rate sensitivity but is very sensitive to adiabatic heating. Consequently, the softening due to adiabatic heating supersedes the hardening effect at dynamic rates in martensite. This could be the reason for the observed initial small drop in the stress at 100/s for CAS steel. But the ductility at 100/s did not decrease, rather increased from the quasi-static rate for CAS steel. In fact, the increase was greater in the post-necking deformation where due to localized temperature rise, the localized necking behavior is believed to have diffused. Similar results of a decrease in the strength of martensite at higher strain rates with an increase in ductility have been reported by Wang et al.[17] Importantly the strength of the CAS steel did not decrease with an increase in strain rate beyond 100/s. On the contrary, at strain rates beyond 100/s, the contribution from the work hardening of the ferrite, which is of the significant fraction in the microstructure, intensifies enough to supersede the softening effect due to adiabatic heating. As a result, the strength increases when the strain rate is increased beyond 100/s. The CAL and CHCL steel microstructures were composed of a large fraction of ferrite (~ 80 pct) because of which the hardening due to strain rate sensitivity was significantly high compared to the softening due to adiabatic heating.
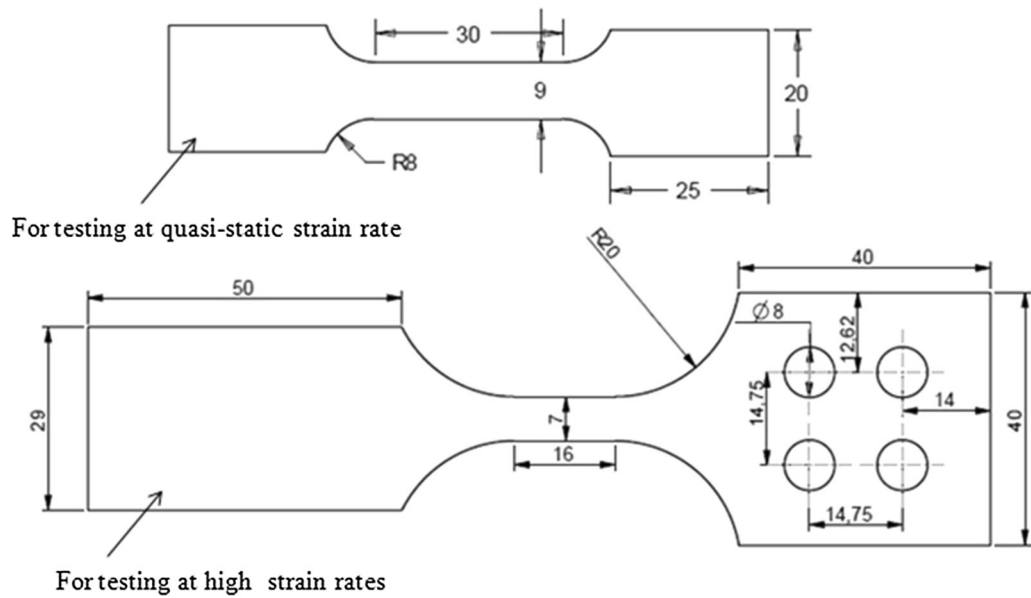
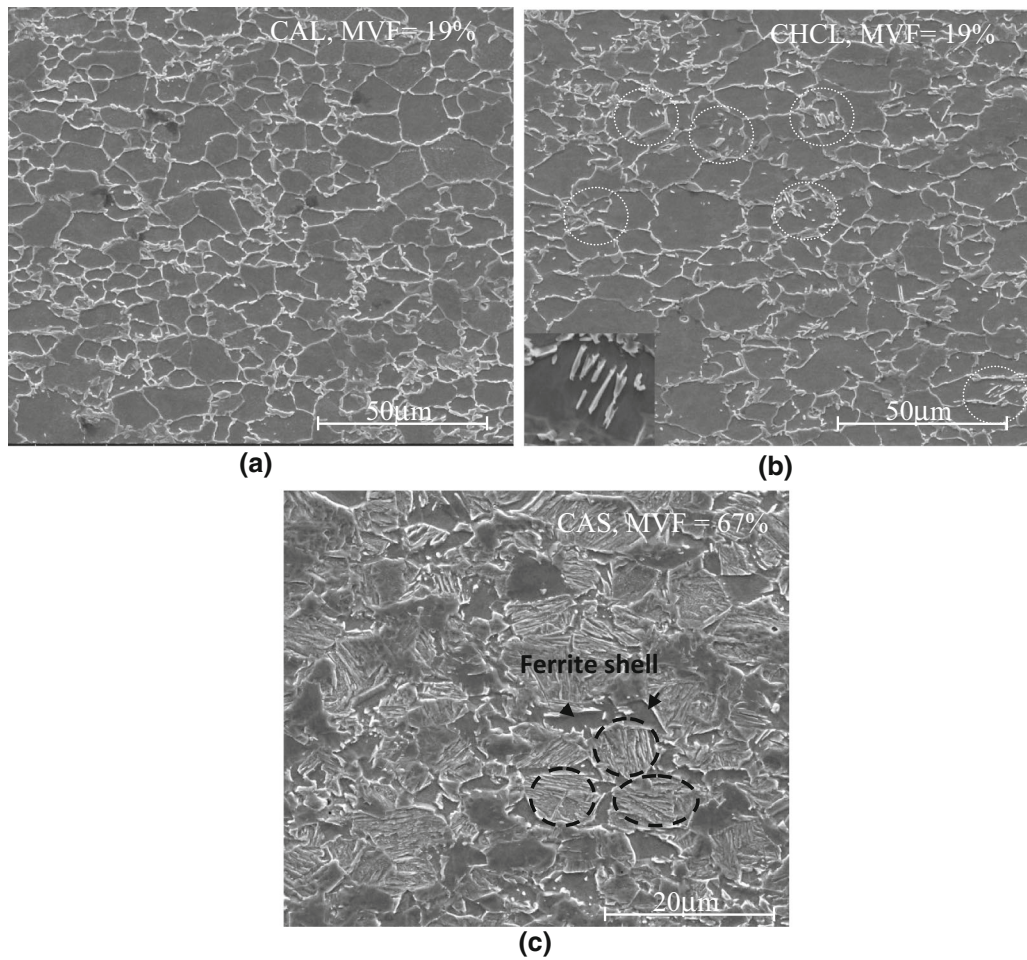Fig. 2—Specimen dimension for quasi-static and tensile tests. All dimensions are in mm.

Fig. 3—Microstructures obtained after processing of as-received steel through (*a*) CAL, (*b*) CHCL, circles are used to highlight the in-grain martensite and high magnification inset image showing in-grain martensite, and (*c*) CAS, circles are used to highlight core martensite surrounded by ferrite shell, indicated by arrows.

Consequently, the strain rate sensitivity also increased positively at high strain rates for CAL and CHCL steel.

In spite of poor strain rate sensitivity of CAS steel, its energy absorption ability is excellent. Figure 8 shows the energy absorbed by the steels at different strain rates when calculated from their true stress–strain curves up to (a) ultimate tensile strength and (b) 10 pct deformation. Since the uniform elongation of CAS was below 10 pct at some strain rates, so the energy values were calculated till the uniform deformation for all the cases. The CAL and CHCL steels although showed higher energy when calculated up to UTS till 200 s^{-1} strain rate, but it dropped after that due to a decrease in uniform elongation. CAS steel, on the other hand, showed a monotonic increase in the energy absorption capacity. Even when calculated up to 0.1 true strains, CAS steel possessed the highest energy absorption values. For automotive application, the components are designed in such a way that the materials do not experience more than 10 pct deformation even in a crash instance. Therefore, with reference to crashworthiness, CAS steel shows the highest performance in terms of toughness, mainly at high strain rates.

C. Strain Hardening Behavior Under Various Strain Rate Conditions

The flow curves of these steels obtained during tensile deformation at various strain rates were further analyzed to understand the influence of strain rate on their strain hardening behavior. The instantaneous strain hardening rate $\frac{d\sigma}{d\varepsilon}$ was calculated for all the steels with increasing strain rates. The experimental flow curves

Fig. 4—Engineering stress–strain plots of dual-phase steels produced under various routes at 2.7×10^{-4} s^{-1} strain rate.

were initially fitted with a higher-order polynomial (5th or 6th) for obtaining data smoothening. The fitted curve was smoother than the experimentally obtained flow curves, where the degree of scattering in the experimental data can affect the $\frac{d\sigma}{d\varepsilon}$ calculation. The fitted data points are now used to derive the $\frac{d\sigma}{d\varepsilon}$ at different strain rates. The variation in the strain hardening rates and its behavior with strain provides an in depth idea about the operating deformation mechanisms in the materials. The influence of strain rate on the plastic deformation of these three steels can, therefore, be understood by analyzing the strain hardening characteristics at different strain rates. For better understanding, representative strain hardening rate curves with true strain are shown at two different strain rates of the three dual-phase steels in Figure 9. It clearly shows the (a) the effect of strain rate on the strain hardening rates and (b) the variation in strain hardening rates of three different steels. The strain hardening rates of all the DP steels increase with strain rate. The increase was significant in the initial strain levels, but, at high strains, it saturates with no significant difference between different strain rates.

The plastic deformation in the DP steels is largely controlled by the dislocation generation in the ferrite phase. The hard martensite phase acts as a barrier to dislocation motion and creates sufficient obstacles for the dislocations during their propagation. As a consequence, dislocations pile up in the ferrite phase and create significant back stress, for which high strain hardening rates are achieved. With the increase in the strain rate, more dislocations appear during yielding, which further escalates the back stress. The strain hardening rates thus increase at higher strain rates, during the initial portion of plastic deformation. But with the continuation of plastic deformation (at higher strains), the strain hardening rates drastically decrease and saturate, at all strain rates. This can be attributed to the extensive dynamic recovery in the material at all strain rates which brings down the strain hardening rates.

Apart from the influence of strain rate, the microstructure also plays a major role in the plastic deformation behavior of the DP steels. The three different DP steels also show a distinct change in their strain hardening characteristics at any strain rate. The CAL- and CHCL-processed steel show very little difference in the strain hardening behavior at quasi-static as well as high strain rates. This was probably due to their identical martensite volume fraction in the microstructure. The differences in the martensite spatial distribution and to some extent its subtle difference in the morphology of these two steels do not seem to make (negligible) any appreciable effect on strain hardening
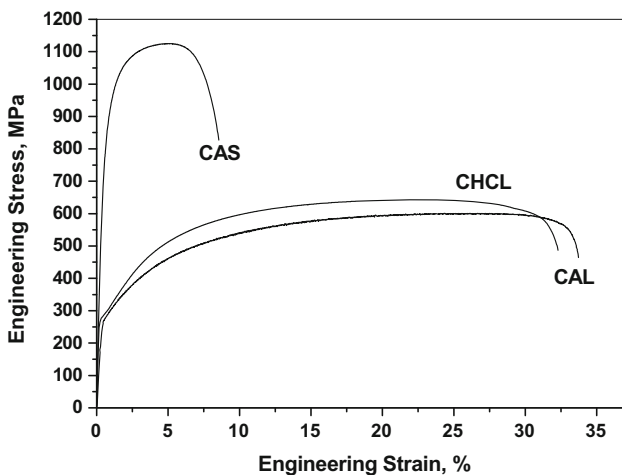
Table II. Tensile Properties of the Selected Steels at Quasi-Static Rate

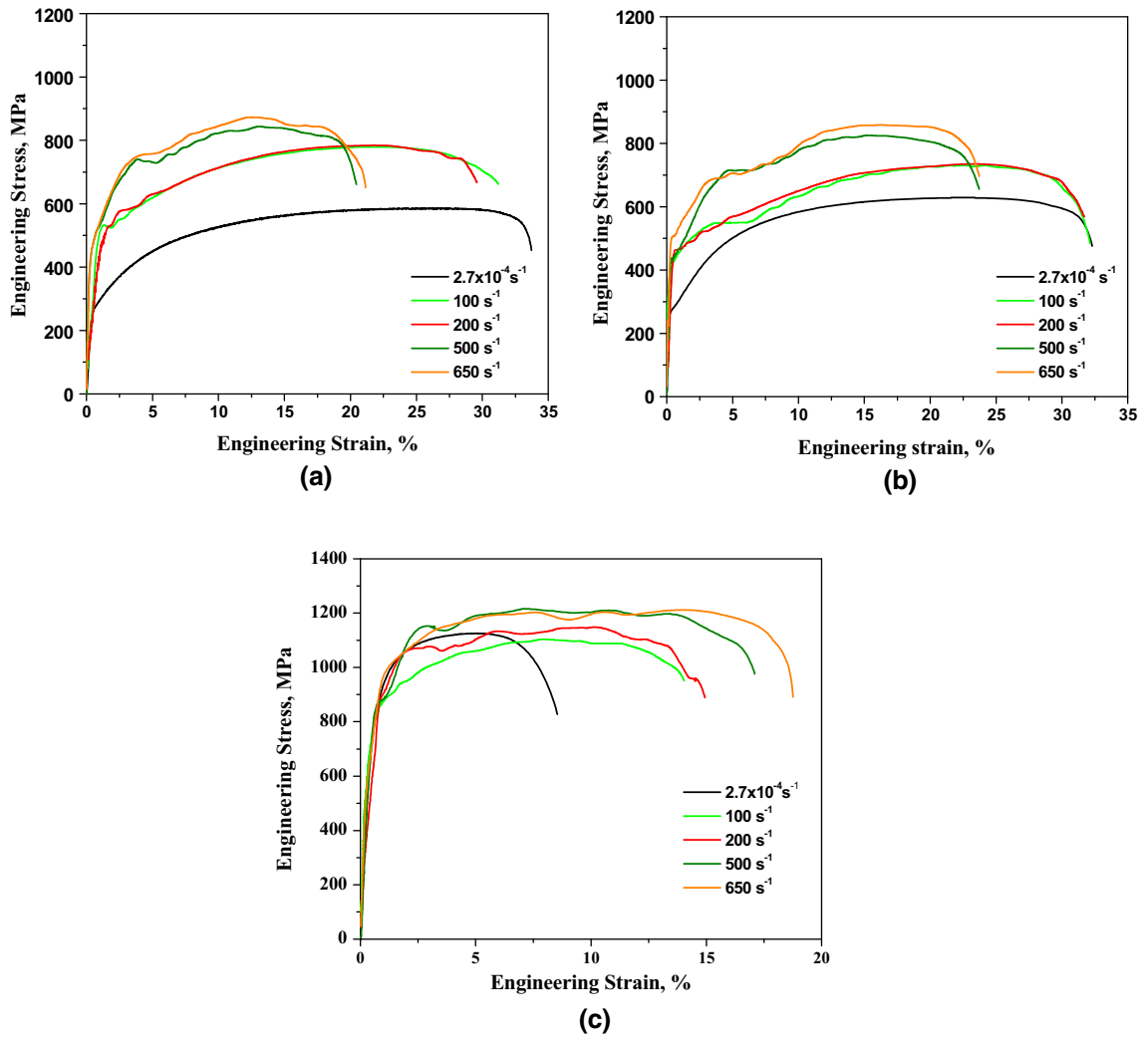| Annealing Route	Yield Strength (MPa)	Ultimate Tensile Strength (MPa)	Percentage Elongation (Pct)
CAL	270	586	26.8
CHCL	279	628	23.9
CAS	800	1125	5.50

Fig. 5—Engineering stress–strain curves under various strain rates for (*a*) CAL, (*b*) CHCL, and (*c*) CAS steels (Color figure online).
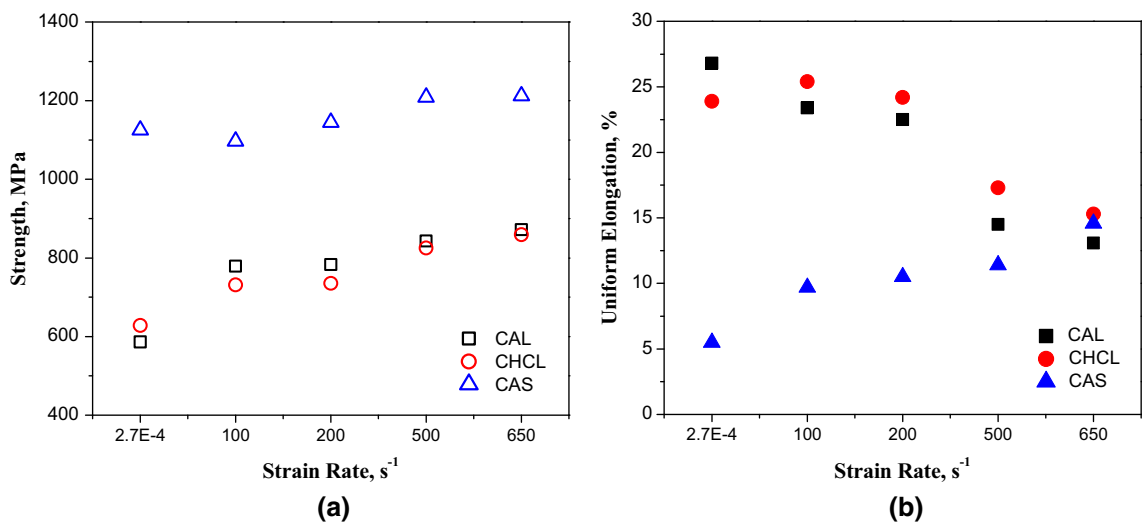

Fig. 6—(*a*) Ultimate tensile strength and (*b*) uniform elongation values of three different steels at different strain rates.
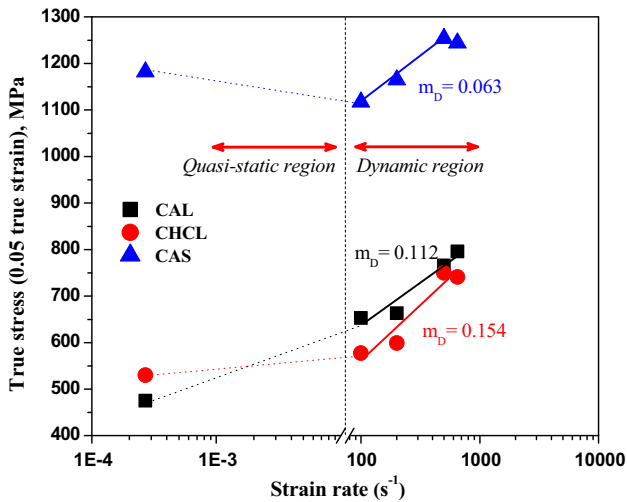
Fig. 7—Strain rate sensitivity of the selected steels at 0.05 true strain level.

characteristics. However, a complete change in the microstructure morphology obtained in CAS steel altered the strain hardening behavior, which was drastically different from others. The presence of higher martensite (~ 67 pct) in CAS has considerably increased the strain hardening rate of the steel, at initial strain levels. It should be noted that the increase in the strain hardening rate of CAS steel at high strain rates is different from the poor hardening characteristics of martensite phase, as discussed in Section III–B–2. The strain hardening rates represent contribution from all the microstructure constituents to the hardening with increase in strain, which includes dislocation–dislocation interaction, interaction of the respective phases, interaction between dislocations with second phase *etc*; whereas the hardening of martensite, as discussed in the previous section, aims to highlight the effect of strain rate exclusively due to martensite phase alone. Modified Crussard–Jaoul (C–J) method was employed to understand more about the strain hardening behavior of these three DP steels when deformed at quasi-static strain rates.[29,30] The $\ln\left(\frac{d\sigma}{d\varepsilon}\right)$ *vs* $\ln \varepsilon$ plots of the three steels at quasi-static condition are shown in Figure 10. This modified C–J method employs Ludwik's equation to represent the flow curves.

Both CAL- and CHCL-processed DP steels showed distinct three strain hardening regimes (stage 1, 2, and 3) of varying slopes.[31] The first stage (stage 1) during yielding mainly comprises dislocation generation in ferrite, which at later stage starts saturating. Because of saturation, the slope is smaller at the second stage (stage 2). The third stage (stage 3) wherein dynamic recovery becomes operational in the ferrite phase and dislocations generated in the ferrite grains assume cell structure.[22] Stage 2 is basically the transition stage between 1 and 3. Also in the stage 3, depending on the microstructure, the martensite can also take part in deformation.[31] Due to considerable ferrite fraction in CAL- and CHCL-processed steels, the above-discussed

changes in microstructure were active during deformation. The transition stage 2 was slightly sharper for CHCL and thus a steeper change from the stage 1 to stage 3 was observed. The different martensite spatial distributions in the two steels seem to reflect on the stage 2 behavior. The partial in-grain martensite spatial distribution present in CHCL steel can be thought to accelerate the dislocation generation during yielding causing the development of higher dislocation density, unlike the presence of martensite at the grain boundaries in CAL steel where the dislocation clustering occurs predominantly close to the grain boundary interface. Due to the presence of in-grain martensite crystals in CHCL, rapid dislocation generation will also occur in the vicinity of ferrite in-grains martensite sites. As a result, more uniform strain partitioning between the ferrite and martensite phases is expected. On the other hand, CAS steel consisting of predominantly martensite hardly displayed any difference in the strain hardening stages. High martensite content appears to be the major cause of inflicting greater damage in the microstructure. Also, the active participation of the ferrite during deformation was apparently less, owing to which negligible stages 1 and 2 were observed.[32,33] Further, due to the presence of higher martensite volume fraction, early martensite activity concurrent with ferrite during deformation is expected. Thus a little deviation in the strain hardening behavior was observed for CAS.

From the above-mentioned observations, it can be inferred that CAS steel due to higher martensite fraction as well as ferrite channeling effect produces much intense plastic deformation. The intensity although drops at higher strain levels. In fact, it drops lower than CAL and CHCL (Figure 10) and this drop further intensifies at higher strain rates. During small strain levels (just after yielding) because of higher strain rate, the matrix experiences a massive dislocation generation and its pile up, causing intensification of the strain hardening rate. But at large strain levels, the effect of adiabatic heating also triggers sufficient softening behavior and limits the strain hardening effect. In CAS steel, the local heating during high strain rate deformations is expected to be distributed uniformly due to the presence of (a) large ferrite–martensite interface area and (b) entrapment of the ferrite, as a channel between martensite packets. As a result, the ferrite is expected to experience greater recovery due to uniform heating of the microstructure at high strain rates. The adiabatic heating would also influence the plastic deformation behavior of martensite due to its softening. In such situation, the strain incompatibility between the two phases would be reduced and result in enhancing the overall plasticity of the steel. This could also be a plausible reason for the observed increase in elongation at high strain rates for CAS steel.

D. Microstructure Characterization After Deformation

1. Microstructure in the vicinity of fracture tip

Microstructures of the deformed specimens were observed on the RD-TD plane near the fractured ends. Figure 11 shows the different void initiation and
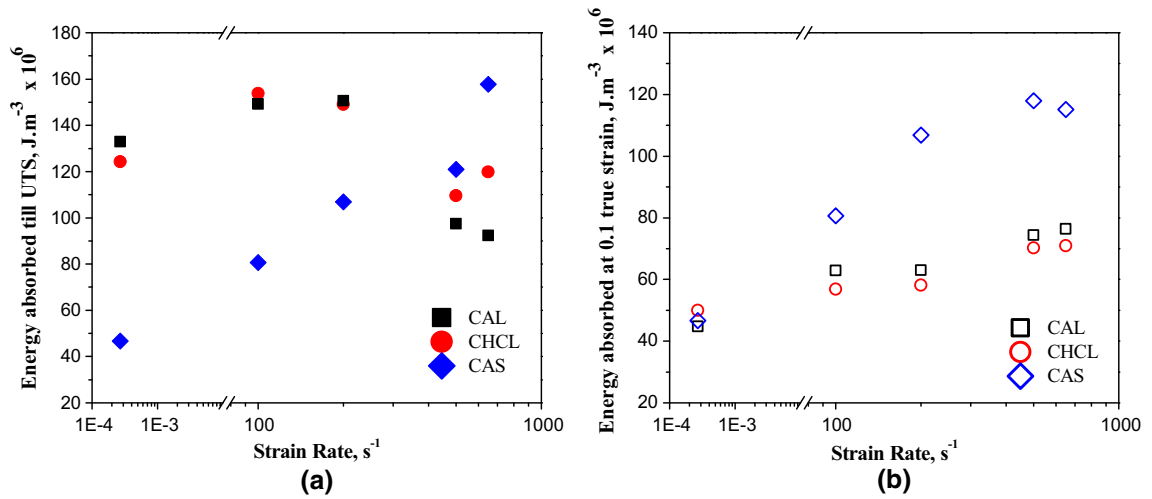
Fig. 8—The energy absorption values of different dual-phase steels at different strain rates when calculated up to (*a*) UTS and (*b*) 0.1 true strain level.
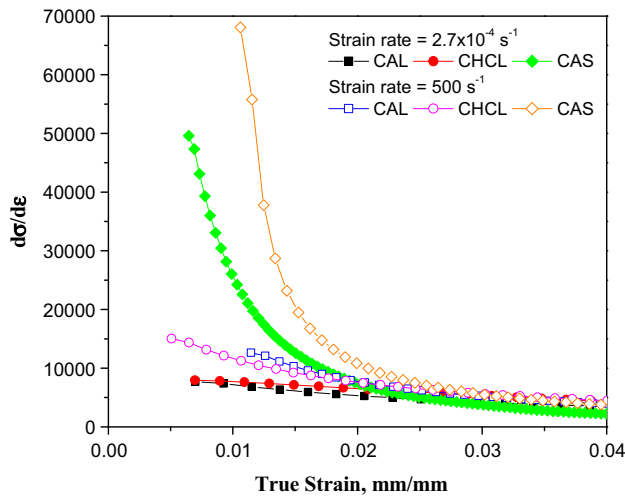

Fig. 9—Instantaneous strain hardening rates of three different dual-phase steels at 2.7×10^{-4} and 500 s^{-1} strain rates.

Fig. 10—Crussard–Jaoul plots of the three different dual-phase steels at quasi-static strain rate.

propagation activities in the three steels at a strain rate of 500 s^{-1}.

The ferrite/martensite inter-phase boundary decohesion was a prominent damage mechanism for the CAL-processed steels at high strain rates. The void initiated at the interface propagates through the interface and builds up to create global damage (Figure 11(a)). CHCL steel also exhibited interface decohesion as the main damage mechanism. But the voids formed in this case were not only initiated at the interface but also at the sites of in-grain martensite. Figure 11(b) shows voids generated at the in-grain martensitic interface site, pointed by the arrow. The microvoids initiated at the in-grain martensite mostly form a spherical void rather than as a macro crack at the grain boundary interface (as seen for CAL). These spherical voids at the in-grain interface grow uniformly and consume higher energy before it coalesces. This can be the possible reason for delaying the fracture process
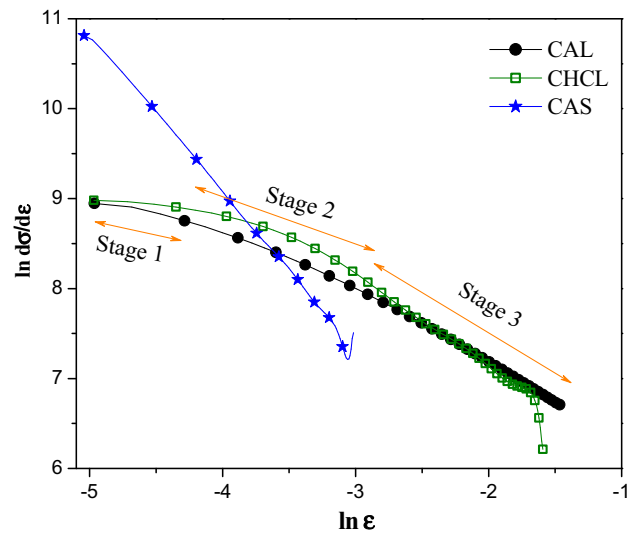
and thus a little higher elongation was always achieved for CHCL compared to CAL at high strain rates. Early fracture of the CAL in comparison to CHCL-processed steel was also reported by Chakraborty *et al.*[10] At the quasi-static strain rate, a subtly observed decrease in elongation in CHCL compared to that of CAL may be attributed to the difference in strain hardening ability of the two steels. One of the possible reasons could be the additional in-grain dislocation generation sites for CHCL giving rise to higher strain hardening response. However, this behavior is still under investigation, and more detailed analysis is required to extract information about the minute change in the elongation at low strain rates.

In the CAS-processed steel, cracks were found to initiate from the martensite inter-lath interface. But interestingly these cracks were arrested at the martensite–ferrite inter-phase boundary due to blunting effect
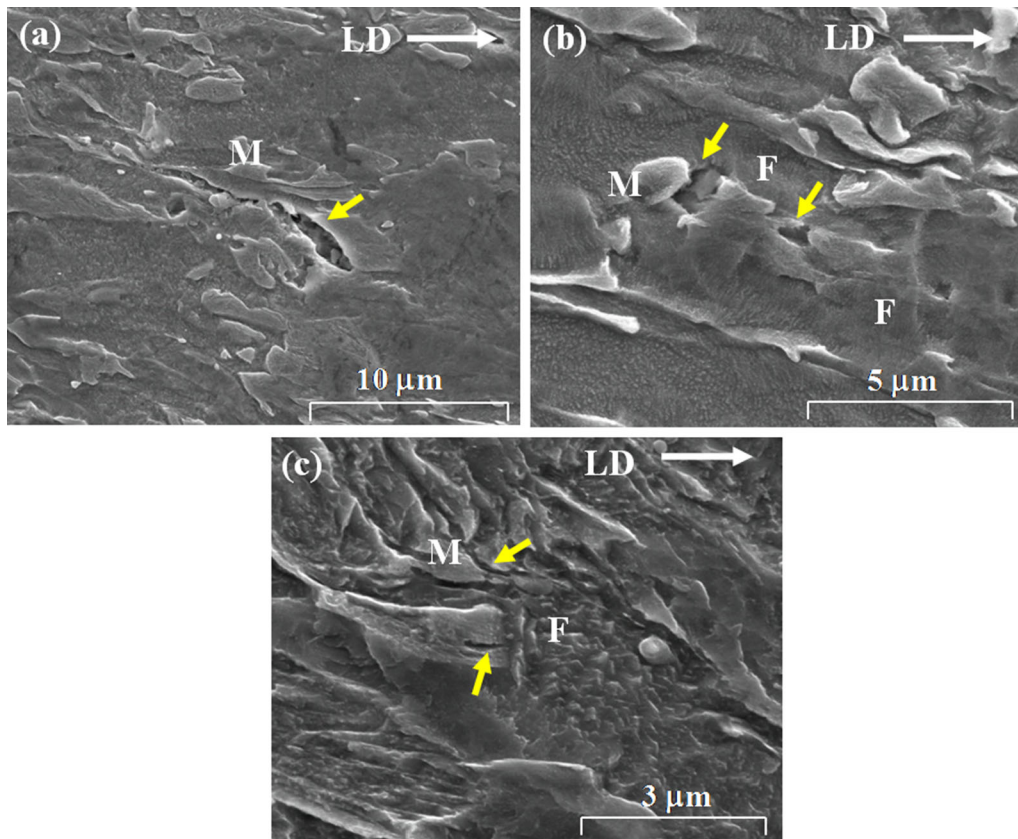
Fig. 11—Micrographs showing micro cracks at ferrite–martensite interface near fracture tip of specimens tested at a strain rate of 500 s^{-1} showing (a) large growth of micro crack in CAL-processed dual-phase steel; (b, c) showing blunting of cracks in ferrite in CHCL and CAS samples, respectively. White arrows indicate tensile loading direction and yellow arrows indicate micro cracks. **F** and **M** indicate ferrite and martensite, respectively.

by the soft ferrite phase (as shown in Figure 11(c)). The blunting effect can be realized as an increase in the crack tip root radius due to plastic deformation when the crack encounters the ferrite grains. Due to the difference in the ability to accommodate strain between the ferrite and martensite, the rate of propagation of cracks in these two phases also differs to a large extent. When these cracks initiate in martensite, they require almost negligible energy to propagate. But on encountering a softer phase, like ferrite, these cracks encounter difficulty in propagating through the ferrite grains. Accompanied by substantial plastic deformation, the crack tip deforms along with negligible propagation. Also, the crack branching due to ferrite posing as an obstacle in the path of these cracks was witnessed in the post-tensile fractured specimens. Even in the event of crack branching, higher energy is consumed to propagate it.

Furthermore, the martensite grains were found heavily deformed in the CAS steel. This confirms the participation of martensite in the deformation process in the CAS steel. The participation of martensite in the deformation process was also earlier reported at quasi-static strain rates.[31] Moreover, at high strain rates, the adiabatic heating largely affects the constituent phases. In CAS steel, this effect was very much prominent. This further enhances the fact that, strain incompatibility between the ferrite and martensite was

small in CAS steel. Therefore, inter-phase boundary decohesion reduced at high strain rate in the CAS steel. At very high-stress levels, the onset of martensite inter-lath interface crack occurs. The growth or propagation of these micro cracks was hindered by surrounding ferrite (core–shell microstructure) and caused its blunting. The occurrence of crack tip blunting results in the enhancement of ductility at high strain rates of deformation.

2. Fractography

The fracture surfaces of three steels under tensile deformation at different strain rates were subjected to fractography analysis under SEM. Typical fractographs at high strain rates are shown in Figures 12(a) through (d). The fracture mechanisms of CAL and CHCL steels were almost identical. In general, their fracture characteristics remained nearly same at both quasi-static as well as high strain rate tensile deformations. Both steels exhibited a well-connected network of voids and dimples on the fracture surface, as shown in Figures 12(a) and (b). However, their ductility at each strain rate studied decreased with increasing strain rates, with CHCL steel showing a somewhat smaller decrease with increase in strain rate (Figure 5).

On the other hand in the CAS steel, extensive shearing of the dimple surface producing smeared facet features
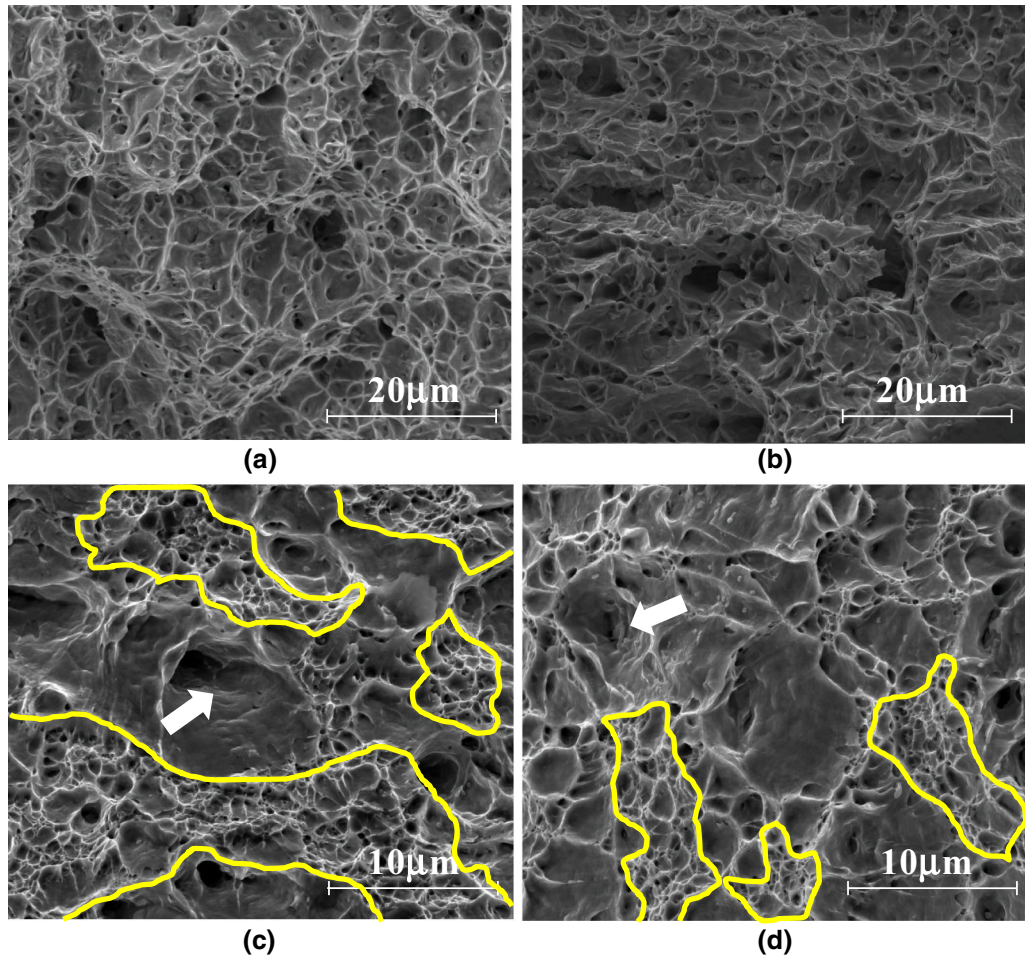
Fig. 12—Fractographs of the selected steels at different strain rates. Fractographs of (*a*) CAL and (*b*) CHCL-processed steel at 650/s strain rate. Fractographs of CAS steel at (*c*) 2.7×10^{-4} and (*d*) 650 s^{-1} strain rates, where the demarcated area in yellow shows the void network, and the large dimples are marked with arrows in the fractographs.
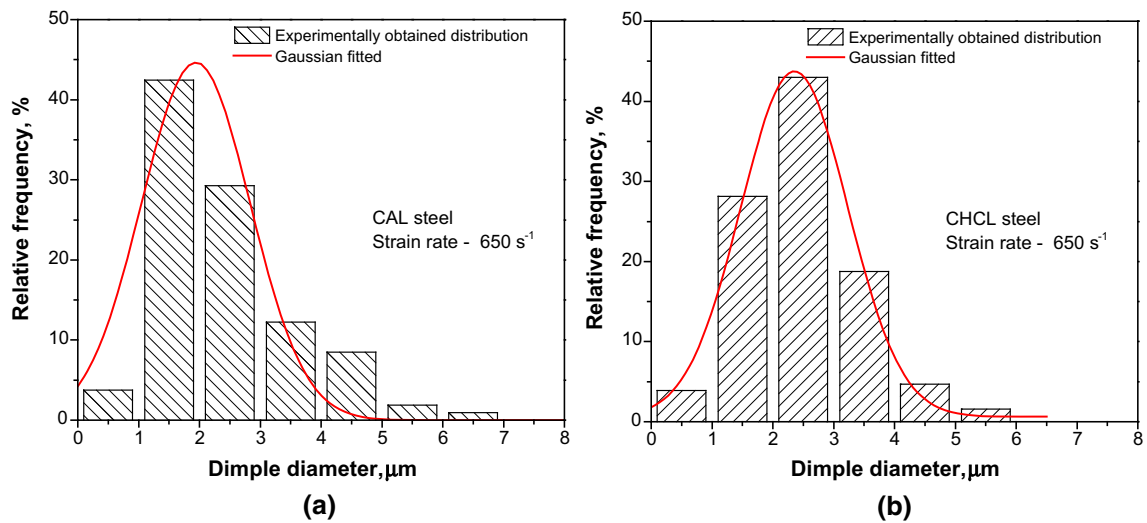

Fig. 13—Distribution of dimple size in the fracture surface of (*a*) CAL and (*b*) CHCL steel when deformed at 650 s^{-1} strain rate.

around the dimple edges was formed, as shown in Figure 12(c). Moreover, a significant number of dimples of considerably larger size than CAL and CHCL are

present in the fracture surface of CAS steel at both the strain rates. The equivalent diameter of the dimples present in the fracture surfaces was measured for all the
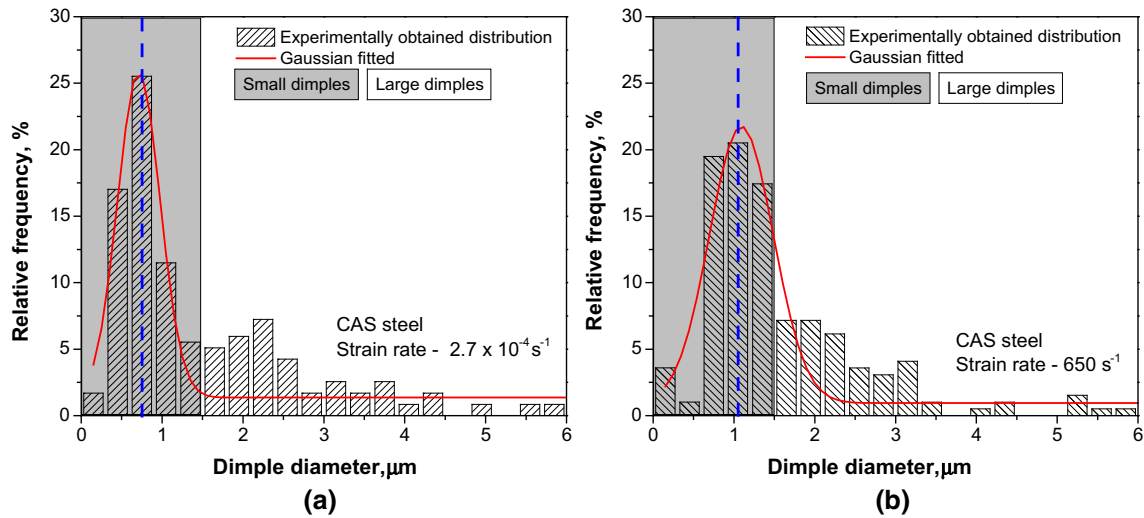
Fig. 14—Distribution of dimple size in the fracture surface of CAS steel when deformed at (*a*) 2.7×10^{-4} and (*b*) 650 s^{-1} strain rates.

steels deformed at various strain rates. The average dimple diameter rates for CAL and CHCL, when deformed at 650 s^{-1} strain rate, were 1.89 ±1.13 μm and 2.03 ± 1.25 μm, respectively. The corresponding dimple size distribution of CAL and CHCL steels at 650 s^{-1} strain rate is shown in Figure 13. A subtle larger dimple diameter size for CHCL explains a detectable improvement in its ductility at high strain rates.

The CAS steel showed some interesting behavior with respect to the quantitative fractography. The morphological differences in the microstructure of CAS steel come into play at high strain rates. Due to the core–shell martensite/ferrite structure in CAS, where martensite is surrounded by ferrite, the local damage initiates like an inter-granular fashion in martensite packets although controlled by the ductile mechanism. Some of the martensite packets which are completely surrounded by ferrite act as floating second hard phase particles within ferrite matrix. The entire interface opens up during fracture leaving behind the impression of the martensite block. This situation prevails almost in equal proportion at quasi-static and high strain rates. In the low strain rate-deformed steel, the fractograph shows a profound network of small voids/dimples, as demarcated in Figure 12(c). For the CAS steel also, the dimple size distribution was measured from multiple fractographs. The distribution of the dimple size of CAS steel at 2.7×10^{-4} and 650 s^{-1} strain rates is shown in Figure 14. The histograms clearly show the dominance of the small voids presence in the fractographs, as shown by the shaded area. The average dimple size was evaluated for the small dimples forming a network and larger size dimples as marked in Figures 12(c) and (d). At quasi-static strain rate, the average size of the dimples in the network of small voids/dimples is 0.87 ± 0.47 μm, whereas the average size at a strain rate of 650 s^{-1} is 1.19 + 0.52 μm. The average size of the larger dimples varied from 4.2 ± 1.97 μm at quasi-static strain rate to 3.8 + 1.53 μm at 650 s^{-1} strain rate. From the quantitative data presented above, the differences in fracture property of these steels could

be better understood. Firstly, compared to CAL and CHCL, the dimple and void network is not uniformly distributed in CAS steel. A network of small voids or dimples exists along with scattered dimples of sufficiently larger size than compared to the uniform dimple network of CAL and CHCL steels. Secondly, with an increase in strain rate, the network of small voids grew to a higher size. This is also the reason for higher ductility of CAS steel at high strain rates.

Considering identical void-initiating sites for CAS at each strain rate, during low rate deformation it can be assumed that most of these sites were activated and microvoids have initiated from them. Due to the complexity of the microstructure, variation of dimple size (a larger shallow + network of small microvoids) across the fracture surface exists. The enhanced plasticity of the phases during high strain rate deformation alters the void nucleation probability. It was seen that martensite deforms to a large extent in the CAS steel when pulled at high strain rate. This brings down the difference in the strain accommodation between the two phases. As a result, the flow of martensite across the inter-phase boundary closes some of the possible void-initiating sites. In a recent work, Das *et al.* reported the increase in the void size of DP600 steel due to the enhanced plasticity of the ferrite phase around the martensite crystal at high strain rates.[22] In that case, the martensite content was around 12 pct with large ferrite grains. Comparing with what is reported in,[22] the plasticity enhancement in ferrite, martensite, or both can affect the void nucleation phenomenon at high strain rates.

IV. CONCLUSIONS

The present study showed a possibility of microstructure engineering to produce high-strength DP ferrite/martensite structure with an improved crashworthiness. It has been shown that morphology of martensite and its spatial distribution is crucial in

attaining a good combination of high strength and ductility, apart from its volume fraction and size. The influence of strain rate on all three DP steels can be broadly summarized as:

(a) Increase in strength with strain rate mainly depended on the volume fraction of martensite present. The CAS steel having high strength due to large martensite volume fraction showed least strain rate sensitivity among all three steels of this study.

(b) The core–shell type microstructure of CAS steel was found effective in increasing the ductility at high strain rates. Ferrite surrounding martensite in CAS steel was observed to restrict the growth of crack emanating from the inter-lath interface of martensite. Adiabatic heating of specimen at high strain rates softens martensite, present in large volume fraction, further aiding in increasing its plasticity. The softening of martensite also results in the reduction of strain incompatibility between the existing phases.

(c) Increase in strain hardening rate at high strain rates was observed for all the three DP steels. CAS steel showed the highest hardening rate among all. The entrapped ferrite within martensite experiences an immense deformation during yielding. This shoots up the overall strain hardening rate of the steel. In-grain martensite in the CHCL steel also contributes to its strain hardening rate which is higher than that of CAL steel even though both the steels possess identical volume fraction of martensite.

(d) The fracture of the all three steels was predominantly ductile in a manner at all strain rates. The in-grain martensite in CHCL enables the formation of deeper voids during fracture at high strain rates, inducing better ductility than that of CAL at high strain rates. CAS steel, on the other hand, shows large dimples due to inter-granular decohesion of the large martensite laths, controlled by ductile fracture mechanisms. Moreover, due to the enhanced plasticity of martensite at high strain rates, the number of probable void nucleation sites was reduced. The reduction in the void nucleation site promoted the growth of voids that have nucleated early, at high strain rates.

REFERENCES

1. D.K. Mondal and R.M. Dey: *Mater. Sci. Eng. A*, 1992, vol. 149, pp. 173–81.
2. Y. Cao, J. Ahlström, and B. Karlsson: *J. Mater. Res. Technol.*, 2015, vol. 4, pp. 68–74.
3. G. R. Speich: *Fundamentals of Dual Phase Steels*, Chicago, USA, 1981, pp. 3–46.
4. R.G. Davies: *Metall. Mater. Trans. A*, 1978, vol. 9A, pp. 671–79.
5. L. Wannman and A. Melander: *Mater. Des.*, 1991, vol. 12 (3), pp. 129–32.
6. R.A. Mohammad and A. Ekrami: *Mater. Sci. Eng. A*, 2008, vol. 477, pp. 306–10.
7. L.V.D.L. Concepción, N.H. Lorusso, and G.H. Svobod: *Proced. Mater. Sci.*, 2015, vol. 8, pp. 1047–56.
8. Z. Jiang, Z. Guan, and J. Lian: *Mater. Sci. Eng. A.*, 1995, vol. 190, pp. 55–64.
9. V. Singh, M. Adhikary, T. Venugopalan, A. Chakraborty, T. Nanda, and B. Ravi Kumar: *Mater. Manuf. Process.*, https://doi.org/10.1080/10426914.2017.1317792.
10. A. Chakraborty, M. Adhikary, T. Venugopalan, V. Singh, T. Nanda, and B. Ravi Kumar: *Mater. Sci. Eng. A*, 2016, vol. 676, pp. 463–73.
11. M. Erdogan and S. Tekeli: *Mater. Charact.*, 2002, vol. 49, pp. 445–54.
12. X. Sun, K.S. Choi, A. Soulami, W.N. Liu, and M.A. Khaleel: *Mater. Sci. Eng. A*, 2009, vol. 526, pp. 140–49.
13. N.J. Kim and G. Thomas: *Metall. Mater. Trans. A.*, 1981, vol. 12A, pp. 483–89.
14. X.J. He, N. Terao, and A. Berghezan: *Met. Sci.*, 1984, vol. 18, pp. 367–73.
15. J. Zhang, D. Hongshuang, Y. Deng, and R.D.K. Misra: *Mater. Sci. Eng. A*, 2015, vol. 627, pp. 230–40.
16. B. Ravi Kumar, N.K. Patel, K. Mukherjee, M. Walunj, G.K. Mandal, and T. Venugopalan: *Mater. Sci. Eng. A*, 2017, vol. 685, pp. 187–93.
17. W. Wang, M. Li, C. He, X. Wei, D. Wang, and H. Du: *Mater. Des.*, 2013, vol. 47, pp. 510–21.
18. S. Oliver, T.B. Jones, and G. Fourlaris: *Mater. Sci. Tech.*, 2007, vol. 23 (4), pp. 423–31.
19. S. Oliver, T.B. Jones, and G. Fourlaris: *Mater. Charact.*, 2007, vol. 58 (4), pp. 390–400.
20. H. Huh, S.B. Kim, J.H. Song, and J.H. Lim: *Int. J. Mech. Sci.*, 2008, vol. 50 (5), pp. 918–31.
21. N.D. Beynon, T.B. Jones, and G. Fourlaris: *Mater. Sci. Technol.*, 2005, vol. 21, pp. 103–12.
22. A. Das, M. Ghosh, S. Tarafder, S. Sivaprasad, and D. Chakrabarti: *Mater. Sci. Eng. A*, 2017, vol. 680, pp. 249–58.
23. ASTM, E-8M: *Standard Test Methods for Tension Testing of Metallic Materials [Metric]*, 1997.
24. P. K. C. Wood and C. A. Schley: *Strain Rate Testing of Metallic Materials and Their Modelling for use in CAE Based Automotive Crash Simulation Tools (Recommendations and Procedures)*, Smithers Publishers, 2009.
25. ISO 26203-2: *Metallic Materials - Tensile Testing at High Strain Rates - Part 2: Servohydraulic and Other Test Systems*, International Standard, 2011.
26. S.K. Paul, A. Raj, P. Biswas, G. Manikandan, and R.K. Verma: *Mater. Des.*, 2014, vol. 57, pp. 211–17.
27. A. Uenishi and C. Teodosiu: *Acta Mater.*, 2003, vol. 51, pp. 4437–46.
28. A. Bardelcik, C.P. Salisbury, S. Winkler, M.A. Wells, and M.J. Worswick: *Int. J. Impact Eng.*, 2010, vol. 37, pp. 694–702.
29. A. Bag, K.K. Ray, and E.S. Dwarakadasa: *Metall. Mater. Trans. A*, 1999, vol. 30A, pp. 1193–1202.
30. C.H. Crussard and B. Jaoul: *Rev. Metall.*, 1950, vol. 42, pp. 589–600.
31. A.G. Kalashami, A. Kermanpur, E. Ghassemali, A. Najafizadeh, and Y. Mazaheri: *Mater. Sci. Eng. A*, 2016, vol. 678, pp. 215–26.
32. Y. Bergstrom, Y. Granbom, and D. Sterkenburg: *J. Metall.*, 2010, https://doi.org/10.1155/2010/647198.
33. H. Ashrafi, M. Shamanian, R. Emadi, and N. Saeidi: *Trans. Indian Inst. Met.*, 2017, vol. 70 (6), pp. 1575–84.